Journal of ELECTRONIC MATERIALS, Vol. 48, No. 1, 2019
https://doi.org/10.1007/s11664-018-6743-2
© 2018 The Minerals, Metals & Materials Society

Efficient Use of Low-Bandgap GaAs/GaSb to Convert More than 50% of Solar Radiation into Electrical Energy: A Numerical Approach

G.S. SAHOO[1] and G.P. MISHRA[1,2]

1.—Device Simulation Lab, Department of Electronics and Communication Engineering, Institute of Technical Education and Research, Siksha 'O' Anusandhan Deemed to be University, Khandagiri, Bhubaneswar, India. 2.—e-mail: gurumishra@soa.ac.in

A recent trend in photovoltaic technology is to aim to enhance the conversion efficiency of this energy harvesting technique. Although multijunction solar cells offer high efficiency, factors such as fabrication cost, cost per watt of energy produced, etc. limit their application. An alternative approach based on a lower-bandgap GaAs/GaSb dual-junction solar cell is proposed herein. For efficient use of longer wavelengths of the solar spectrum, a model for a simple antireflection coating (ARC)-less GaAs/GaSb dual-junction cell with a double back-surface field layer was optimized. The model was simulated using the Silvaco ATLAS technology computer-aided design (TCAD) tool and validated based on parameters such as the quantum efficiency, photogeneration rate, and spectral response. The model predicts conversion efficiency of 54%, better than some reported experimental results.

Key words: Tandem cell, quantum efficiency, spectral response, efficiency, ATLAS, fill factor

INTRODUCTION

The total global energy consumption per year amounts to a fraction of the energy received from the sun in one year.[1] Techniques are therefore being developed and implemented to harvest this solar energy for effective use by mankind. Photovoltaic (PV) cells are emerging as alternatives to harness solar energy, representing a solution to the problems of global warming and fuel scarcity.[1,2] PV cells can convert electromagnetic radiation from the sun directly into electrical energy based on a phenomenon known as the photovoltaic effect.[3]

PV cells based on silicon with its indirect bandgap can achieve conversion efficiency of around 26%,[4] but less than the theoretical limit proposed by Shockley and Queisser.[5] The main reason for such energy loss in a solar cell is the energy mismatch between the incident photons and the bandgap of the material.[1,6,7] PVs based on compound materials from group III–V of the Periodic Table can not only compensate for such losses due to the bandgap mismatch but also provide higher conversion efficiency. Generally, such compound materials are termed direct-bandgap materials, and utilizing the cell stacking technique, the losses can be minimized to a certain extent. Such PVs based on compound materials offer many advantages, including bandgap tunability (by varying the composition of the compound), high photoabsorption (due to their direct bandgap), potential for use in concentrator systems, improved robustness to high-energy rays from space, better photon recycling, good resistance to temperature, and enhanced radiation hardness.[1,8–10] The theoretical efficiency predicted for solar cells based on group III–V compound materials under concentrated solar illumination is 40% for a single junction (1-J), 55% for a dual junction (2-J), 63% for a triple junction (3-J), and 86% for infinitely many junctions.[11,12] To further enhance the conversion efficiency, multijunction (MJ) cells can be considered. The first MJ cell concept was proposed

(Received May 9, 2018; accepted October 16, 2018; published online October 30, 2018)

in 1955 by Jackson, followed by Wolf in 1960.[10] MJ cells are monolithic two-terminal series-connected structures. Based on the background above, note that, as the stacking of the cell or the number of junctions is increased, its efficiency increases significantly. However, this efficiency enhancement is not significant compared with the increased cost and fabrication complexities of such MJ cells. Hence, the dual-junction (DJ) monolithic structure is preferred over expensive 3-J and 4-J structures.[6,7] To make a DJ structure with efficiency on a par with MJ structures, consideration must be given to the material selection (with a proper bandgap to absorb a large range of the spectral band) and optically transparent interconnection (without absorption or recombination losses).[13,14]

It was recently reported that high-efficiency 2-J InGaP/GaAs cells exhibited conversion efficiency of 30.3%[15,16] (under 1 sun AM1.5G illumination) and 32.6%[17] (under AM1.5D, 1000 sun condition), while lattice-mismatched GaAs/GaSb 2-J cells were reported to exhibit conversion efficiency of 32.6% under AM1.5D at only 100 suns.[18] Sahoo et al. presented a metamorphic InGaP/GaAs dual-junction (DJ) model with conversion efficiency of 30.40% (under 1 sun AM1.5G illumination), a lattice-matched InGaP/GaAs DJ model with efficiency above 43% using a hetero tunnel junction (under 1000 sun AM1.5G illumination), and 33.3% under 100 suns using a wide-bandgap tunnel junction.[19–21] Many such reports are available in literature, based on designs using TCAD software and helping to advance the study of solar cells.[22–24]

NUMERICAL MODELING AND SIMULATION

Material Selection for Proposed Device

Takamoto et al.[25] used three layers of active material, utilizing the spectrum up to only 1400 nm. Steiner et al.[26] used four layers of active material, utilizing the spectrum up to 1800 nm to achieve very high efficiency. However, application of two layers of active material can utilize the spectrum up to 1800 nm while minimizing absorption and recombination losses (due to the smaller number of tunnel junctions). To examine this possibility, one must first select a bottom cell material, showing a spectral response up to 1800 nm, which can be achieved by using Ge or GaSb. As Ge is an indirect-bandgap material,[27] we chose GaSb, as it has the capability to extend the absorption edge towards the infrared region of the spectrum (up to 1800 nm).[28] The direct-bandgap nature of GaSb also helps it to achieve higher photogeneration compared with Si or Ge[28] as well as to generate multiple electron–hole pairs (EHPs) through carrier multiplication phenomena.[29–32] Its advanced fabrication technology with low processing cost, weak temperature dependence, high refractive index, and enhanced radiation hardness make GaSb a potential candidate next-generation solar cell material.[28,32,33] Thermal annealing can increase the radiation hardness of GaSb further.[33]

In the work presented herein, the thicknesses of the different layers and the materials used in the simulations were chosen based on different articles.[20,34–36] The proposed device under test is presented schematically in Fig. 1. A GaAs/GaSb tandem cell was built on a virtual GaSb substrate, where the active part of the top cell consists of GaAs while the bottom cell is made of GaSb. Both active layers were interconnected via a GaAs/GaAs tunnel junction for improved tunneling performance.[37] The properties like the lower surface recombination and higher electric field near the GaAs/GaAs tunneling junction also help to improve the performance of the cell. With its bandgap of 1.42 eV, the top cell utilizes the shorter-wavelength portion of the spectrum (from 300 nm to 900 nm) and bypasses the rest towards the bottom cell.[38] With its lower bandgap of (~ 0.72 eV to 0.8 eV), GaSb[38] absorbs a maximum number of photons in the spectrum with a cut-off wavelength of 1800 nm.

A tunneling phenomenon takes place in the tunnel region with the help of spatial transport phenomena. The proposed model utilizes the nonlocal band-to-band (B2B) tunneling effect to calculate the tunneling current. This nonlocal B2B tunneling depends on a few important parameters such as the longitudinal energy (E), transverse energy (E_T), and tunneling probability [$T(E)$].[39]

In the formulation of the tunneling current, meshing plays a vital role. A special quantum mesh

Contact			
Top Window	$In_{0.49}Ga_{0.51}P$	30nm	$p=2\times10^{18}cm^{-3}$
Top Emitter	GaAs	50nm	$p=2\times10^{18}cm^{-3}$
Top Base	GaAs	550nm	$n=7\times10^{16}cm^{-3}$
Top BSF1	$In_{0.5}(Al_{0.7}Ga_{0.3})_{0.5}P$	30nm	$n=2\times10^{17}cm^{-3}$
Top BSF2	$In_{0.5}(Al_{0.7}Ga_{0.3})_{0.5}P$	30nm	$n=2\times10^{18}cm^{-3}$
TJ	GaAs	25nm	$n=5\times10^{19}cm^{-3}$
TJ	GaAs	25nm	$p=3\times10^{19}cm^{-3}$
Bot Window	$Al_{0.7}Ga_{0.3}Sb$	40nm	$p=2\times10^{18}cm^{-3}$
Bot Emitter	GaSb	500nm	$p=2\times10^{17}cm^{-3}$
Bot Base	GaSb	2µm	$n=2\times10^{18}cm^{-3}$
Bot BSF	$In_{0.5}(Al_{0.7}Ga_{0.3})_{0.5}P$	500nm	$n=5\times10^{19}cm^{-3}$
Substrate	GaSb	500nm	$n=1\times10^{18}cm^{-3}$
Contact			

Fig. 1. Schematic of the proposed GaAs/GaSb-based DJ model.

is used in the tunneling region of the tandem cell. In the initial stage of the simulation, the light propagation and absorption mechanisms are modeled in the ATLAS environment to calculate the optical intensity profile of the device, which is then converted to a photogeneration rate with the help of the carrier continuity equation. Light propagation can be described based on many physical methods. In this case, the ray-tracing (RT) method was used for light propagation, ignoring coherent and diffraction effects. RT uses the real component of the complex refractive index for the calculation of the optical intensity and the imaginary component for the calculation of the new carrier concentration at each grid point. A graph of the complex refractive index is shown in Figs. 2 and 3, being taken from different literature reports and databases.[40–44]

An electrical simulation was carried out with the help of Blaze to calculate the terminal current. Blaze is a general-purpose two-dimensional (2D) device simulator for group III–V and II–VI materials and devices with position-dependent band structures. A few additional physics-based model such as the Shockley–Read–Hall (SRH), concentration-dependent low-field mobility (CONMOB), Auger, and optical recombination (OPTR) models were also applied to calculate the carrier mobility and radiative and nonradiative recombination associated with the cell. To determine the photoresponse of the cell, the optical generation model was applied. Finally the Silvaco numerical tool was used to solve the Poisson and carrier continuity equation, considering the drift–diffusion model for the bulk and thermionic emission for hetero materials to determine the device parameters.

Combining all these effects and physical models, the current densities were calculated as

$$\overrightarrow{J_n} = KT_L\mu_n\nabla n - q\mu_n n\nabla\left(\Psi + \frac{KT_L}{q}ln\gamma_n + \frac{\chi}{q} + \frac{KT_L}{q}ln\frac{N_C}{n_{ir}}\right), \quad (1)$$

$$\overrightarrow{J_p} = KT_L\mu_p\nabla p - q\mu_p p\nabla\left(\Psi - \frac{KT_L}{q}ln\gamma_p + \frac{\chi + E_g}{q} - \frac{KT_L}{q}ln\frac{N_v}{N_{ir}}\right). \quad (2)$$

The values of the important material parameters (such as the bandgap, electron affinity, permittivity, lattice constant, electron–hole mobility, and their lifetimes) used in the calculation of the cell characteristics were taken from Ref. 45. The materials GaAs and GaSb have a huge difference in lattice constant. Such a large lattice mismatch between the subcell materials (GaAs and GaSb) may lead to formation of threading dislocation (TDs) or misfit dislocation (MDs).[46–52] Many researchers have investigated the impact of the threading dislocation density (TDD) on the performance of group III–V solar cells.[53–59] These dislocations propagate into the photoactive cell region and deteriorate the carrier lifetime by reducing the material quality and diffusion length.[50,51] Indeed, one can say that such dislocations will give rise to a large number of recombination centers in the cell, degrading the overall performance of the cell by minimizing both the open-circuit voltage and short-circuit current.[46,51]

There are many well-established methods to control the TDD. These include insertion of various intermediate group III–V layers to form compositionally graded buffers, strained-layer superlattices, insertion of proper buffer layers between the heteroepitaxial layers, and use of thermal annealing.[49,52] In general, to overcome this problem, epitaxy can be performed on both sides of the wafer. Another means of eliminating the TDD is to grow a lattice-matched layer on one side and a lattice-

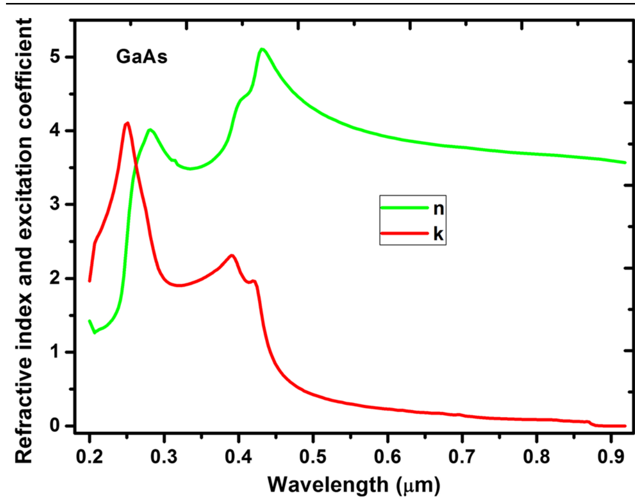

Fig. 2. Complex refractive index of GaAs.

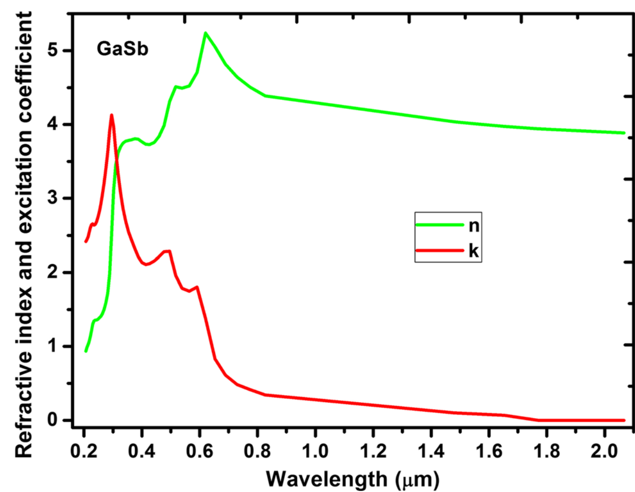

Fig. 3. Complex refractive index of GaSb.

mismatched layer on the other side. The conversion efficiency was calculated to be 42.3% when utilizing the latter method to control the TDD.[60] In the proposed modeling, this technique was again applied to eliminate the chance of threading generation and misfit dislocations. In case of greater lattice mismatch (e.g., 7.8% between GaSb and GaAs), some new growth modes have been developed recently, namely the interfacial misfit dislocation (IMF),[61–63] dislocation filtering layer,[64] and RIBER COMPACT 21 DZ solid-source molecular beam epitaxy (MBE) techniques.[65] Among these, the IMF technique offers a buffer-free approach to obtain high-quality monolithic GaSb grown on an GaAs substrate. In this process, the periodic 90° misfit dislocations self-organize at the heterointerface to relieve the strain energy for a particular growth parameter, growth window, and critical thickness.[66] As a result, a fully relaxed GaSb epilayer with very low TDD ($< 10^5$ cm^{-2}) is obtained. The interested reader can refer to Ref. 66 for details on the IMF growth technique. The proposed device can be fabricated using the IMF growth technique to ensure an allowable TDD of $< 10^5$ cm^{-2}.

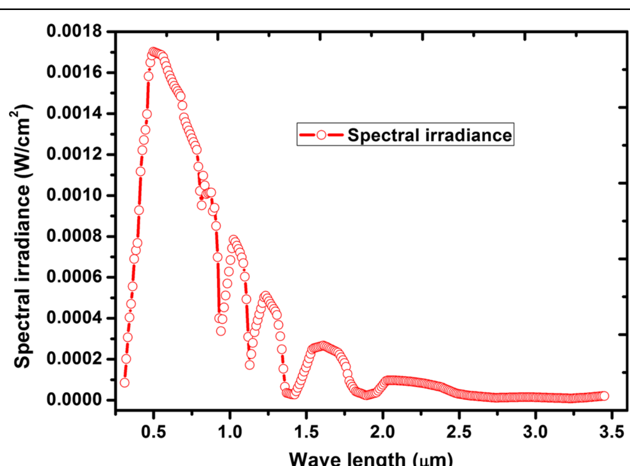

Fig. 4. Spectrum used to illuminate the cell.

RESULTS AND DISCUSSION

The simulations were verified by comparison with analogous characteristics reported previously in literature.[20,34,35,37] The simulations were performed using the American Society for Testing and Materials (ASTM) certified AM1.5G global spectrum in the Silvaco ATLAS device simulator. The standard spectrum (1000 W/m^2) used to illuminate the cell in the simulations is shown in Fig. 4. Depending on

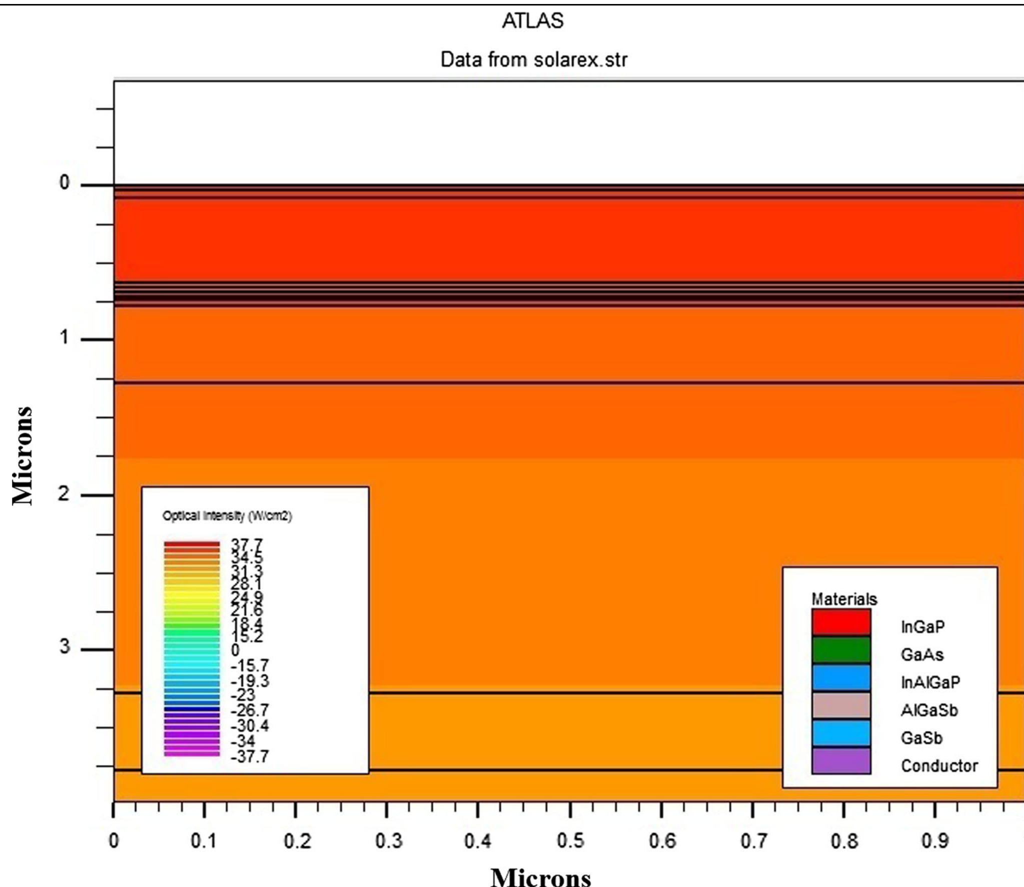

Fig. 5. Optical intensity developed across each layer of the proposed model.

the location, weather, and absorption in different layers of the atmosphere,[20,67] this spectral power distribution may vary at different wavelengths. On a normal day, nearly 10^{17} photons irradiate a surface area of 1 cm^2 each second.

Important photoactivity and electrical parameters of the cell such as the internal quantum efficiency (IQE), external quantum efficiency (EQE), open-circuit voltage (V_{oc}), short-circuit current density (J_{sc}), conversion efficiency (E_{ff}), and fill factor (FF) were estimated using the Silvaco ATLAS TCAD tool. All of these cell parameters depend on the optical intensity, i.e., the amount of solar light illuminating the cell. The materials used in the proposed device exhibit different optical properties, hence the optical intensity varies in each, as illustrated in Fig. 5. The variation in V_{oc} with increase in the amount of sunlight can be represented by

$$V_{oc}^{'} = \frac{nKT}{q}\ln\left(\frac{XI_{SC}}{I_0}\right) = V_{oc} + \frac{nKT}{q}\ln(X). \quad (3)$$

Effect of Varying the Thickness of the Bottom Base Layer

The low-bandgap GaSb helps to generate a greater photocurrent. The thickness of the active base layer is a critical parameter for the current production and voltage preservation of an individual cell. As shown in Fig. 6, variation of the base layer thickness had no effect on the E_{ff} and J_{sc} values of the cell.

Effect of Varying the Thickness of the Top Base Layer

Figure 7 shows the variation in the efficiency and short-circuit current density for the proposed model. The thickness of the top base was varied from 0.6 μm to 2.2 μm. In this range, it was found that both the efficiency and short-circuit current density showed a significant improvement up to thickness of 2.05 μm. However, when the thickness of the base layer exceeded this value, the open-circuit voltage was degraded, decreasing the efficiency of the cell (Table I). Therefore, the thickness of the top base was kept at 2.05 μm in further analysis.

Effect of Varying the Doping Concentration in the Top Base Layer

It is well known that the doping concentration plays a critical role in the depletion width of a *pn* junction. The lower the doping concentration, the greater the depletion width, which favors the operation of solar cell devices. Figure 8 clearly shows that, when the doping concentration was low, the current density increased. However, increasing the doping concentration increased the open-circuit voltage (Table II). Therefore, for a moderate doping

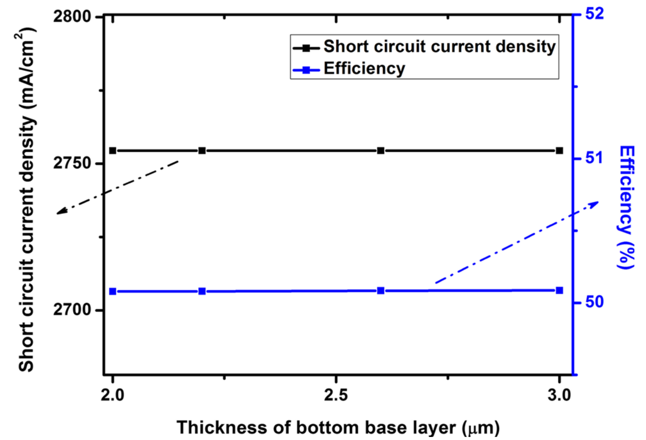

Fig. 6. Effect of varying the bottom base layer thickness on the efficiency and short-circuit current density.

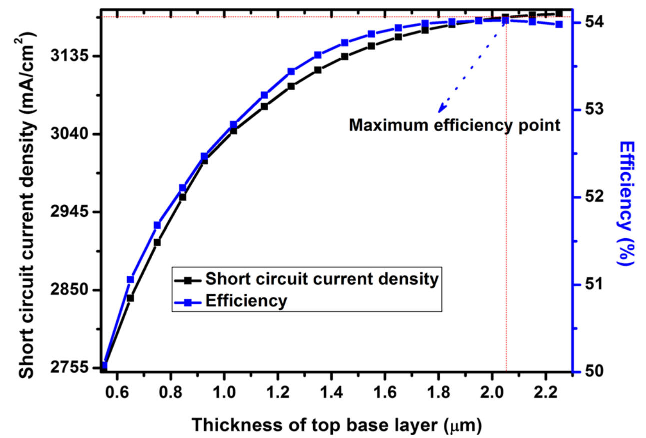

Fig. 7. Effect of varying the top base thickness on the efficiency and short-circuit current density.

concentration ($7 \times 10^{16}/cm^3$), with moderate short-circuit current density and open-circuit voltage (2.24 V), the device showed high efficiency (54.025%).

Effect of Varying the Thickness of the Tunnel Junction

Based on the results of the analysis described above, we fixed the thickness of the bottom base at 2 μm and that of the top base at 2.05 μm with doping concentration of $7 \times 10^{17}/cm^3$. Next, the thickness of the tunnel interconnect must be determined, as it plays an important role in the evaluation of the cell performance.[19,20,35,37] The thickness of the *n*-tunnel layer was varied while keeping the thickness of the *p*-tunnel layer at 0.025 μm. The results revealed that the device showed higher efficiency when the thickness of the *N*-tunnel layer was 0.025 μm (Fig. 9). Then, fixing the *n*-layer

Table I. Effect of varying the thickness of the top base on the open-circuit voltage

Thickness of top base layer (μm)	Open-circuit voltage, V_{oc} (V)
0.55	2.26
0.65	2.26
0.75	2.26
0.85	2.25
0.95	2.25
1.05	2.25
1.15	2.25
1.25	2.25
1.35	2.25
1.45	2.25
1.55	2.25
1.65	2.25
1.75	2.25
1.85	2.25
1.95	2.25
2.05	2.24
2.15	2.24
2.25	2.24

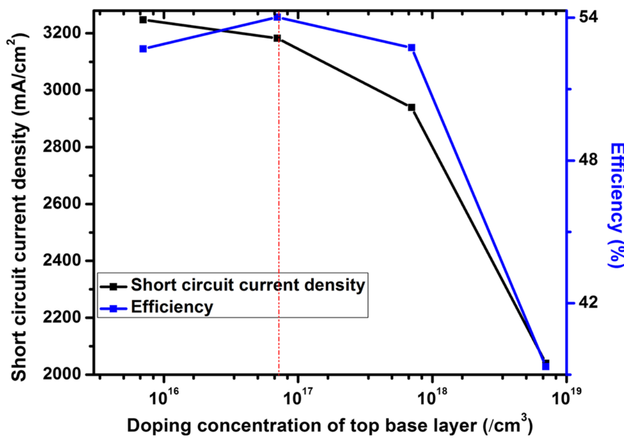

Fig. 8. Effect of doping concentration in the top base layer on the efficiency and short-circuit current density.

Table II. Effect of varying the doping concentration on the open-circuit voltage

Doping concentration (/cm³)	Open-circuit voltage, V_{oc} (V)
7×10^{15}	2.186
7×10^{16}	2.2497
7×10^{17}	2.277
7×10^{18}	2.29

thickness at 0.025 μm, the p-layer thickness was varied. The results showed that a thickness of 0.030 μm gave the highest device efficiency of 54.14% (Fig. 9).

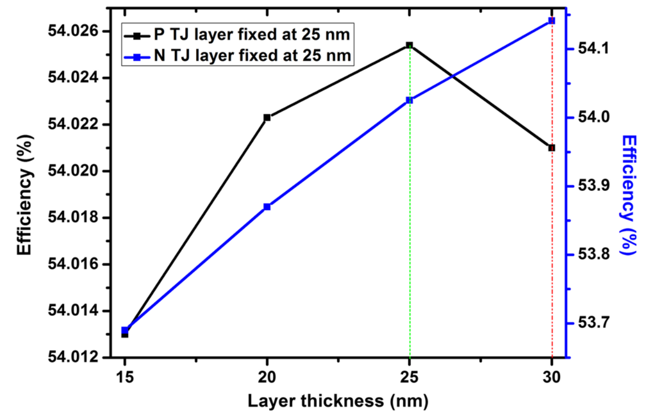

Fig. 9. Effect of the thickness of the tunnel layer on the efficiency and short-circuit current density.

Evaluation and Discussion of Different Performance Parameters of the Cell

To evaluate the performance of a given cell, it is important to study its spectral response, i.e., how photons of different wavelengths contribute to the short-circuit current. With its bandgap of 1.42 eV, the top GaAs cell exhibits a lower photogeneration rate, resulting in a lower photocurrent. The top GaAs cell can utilize the spectrum up to a cutoff wavelength of 900 nm, while the rest of the spectrum is left for the bottom cell (as shown in Fig. 10). It can also be seen from Fig. 10 that the optimized top cell showed a sharp increment in both the available photocurrent and cathode current. This is due to the increased thickness of the base layer.[2] The lower-bandgap material absorbs photons having energy greater than or equal to its bandgap energy. Therefore, GaSb absorbs all photons up to 1800 nm. Thus, the active GaSb layer produces a higher photocurrent, hence the photogenerated current increases in the bottom cell, as shown in Fig. 11.

The current–voltage (I–V) characteristic of the proposed cell is shown in Fig. 12, revealing higher short-circuit current density of 31.57 mA/cm^2 and 3182.66 mA/cm^2 and moderate open-circuit voltage of 1.97 V and 2.25 V for 1 sun and 1000 suns, respectively. These high current and moderate voltage values are achieved due to the use of low-bandgap GaAs and GaSb as the active layers of the cell. Mathematically, the short-circuit current density J_{sc} can be calculated as[19,20]

$$J_{sc} = \int_{\lambda 1}^{\lambda 2} q\phi(\lambda)\mathrm{EQE}(\lambda)\,d\lambda, \quad (4)$$

where $\phi(\lambda)$ is the photon flux, J_{sc} is the short-circuit current density, λ is the wavelength, q is the charge on the electron, and EQE(λ) is the external quantum efficiency of the cell.

The open-circuit voltage can also be expressed as[19,20]

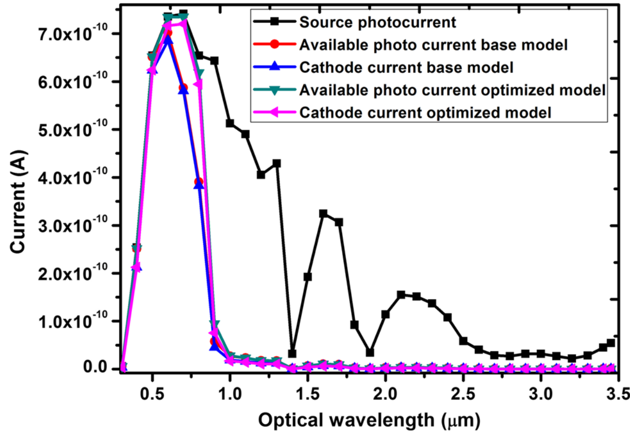

Fig. 10. Spectral response of the top cell.

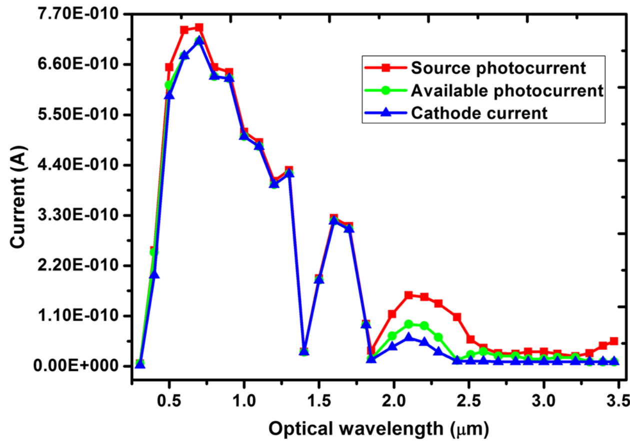

Fig. 11. Spectral response of the bottom cell.

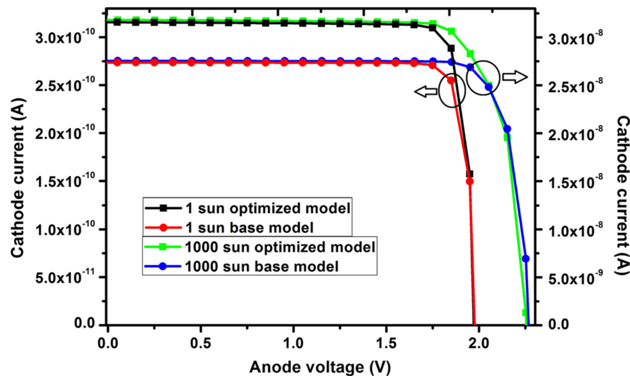

Fig. 12. Open-circuit voltage versus short-circuit current density for 1 sun and 1000 suns.

$$V_{oc} = \frac{nKT}{q} \ln\left(\frac{I_L}{I_0} + 1\right), \tag{5}$$

where I_L is the photocurrent generated by the light, I_0 is the dark saturation current, n is the ideality factor of a diode, T is the temperature, and K is the Boltzmann constant.

The photogeneration rate plays an important role in the determination of the performance of the cell, representing the amount of photons generated across the cell under irradiation. A higher photogeneration rate provides an opportunity to reach higher efficiency,[39] which also increases the photocurrent of the cell. The photogeneration in a cell depends on the spectrum of the illuminating light and the properties of the materials. The photogeneration associated with each grid point can be calculated by integrating the generation rate. Mathematically, the generation rate is given by[20]

$$G = \eta_0 \frac{P\lambda}{hC} \alpha e^{-\alpha y}, \tag{6}$$

where G is the photogeneration rate, P is the intensity of the illuminating ray, y is the distance moved by the ray, h and C are general physical constants, and η_0 is the internal quantum efficiency. The absorption coefficient α is given by[39]

$$\alpha = \frac{4\pi K}{\lambda}\, 10^7 \text{ cm}^{-1}, \tag{7}$$

where K is the excitation coefficient of the material. The absorption coefficient of GaAs and GaSb is shown in Fig. 13.

The generation of photons in each layer of the base and for the optimized model is shown in Fig. 14 for 1 sun and 1000 suns. It can be concluded from Fig. 14 that, as the number of suns increases, so does the photogeneration rate. The proposed architecture also shows a higher photogeneration rate compared with other results reported in literature.[20,34,35] Depending on the absorption coefficient and the available solar radiation, the photogeneration varies throughout the structure. A different absorption coefficient and low carrier scattering in the back-surface field (BSF) region will result in a different photogeneration rate. The high recombination rate of generated carriers in the tunnel interconnect is reflected in Fig. 14 with lower photogeneration.

The performance of the proposed DJ cell was also evaluated by examining the quantum efficiency curve. From this curve, the electrical sensitivity of the device can be calculated as the percentage of free charge carriers at the terminals in the illuminated condition. The quantum efficiency (QE) is then the number of charge carriers collected at the terminals, thus being a function of the intensity and flux distribution of the light source, the reflectance and interference near the surface, and the operating temperature.

The QE can be evaluated in many ways, e.g., as the external quantum efficiency (EQE) or internal quantum efficiency (IQE). Figures 15 and 16 show the EQE and IQE of the proposed cell versus wavelength.

For given wavelength λ, the EQE is defined as[19,20]

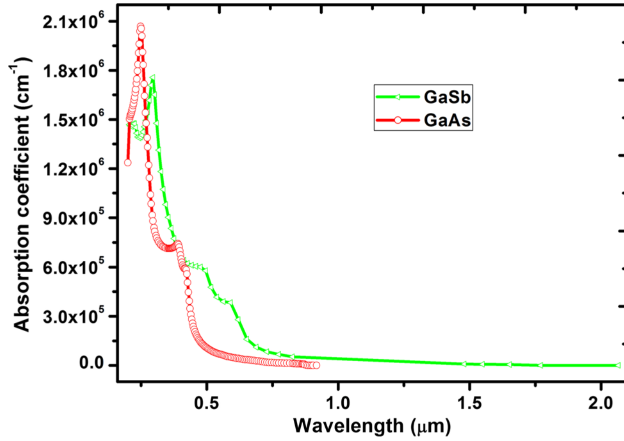

Fig. 13. Absorption coefficient of GaAs and GaSb for different wavelengths.

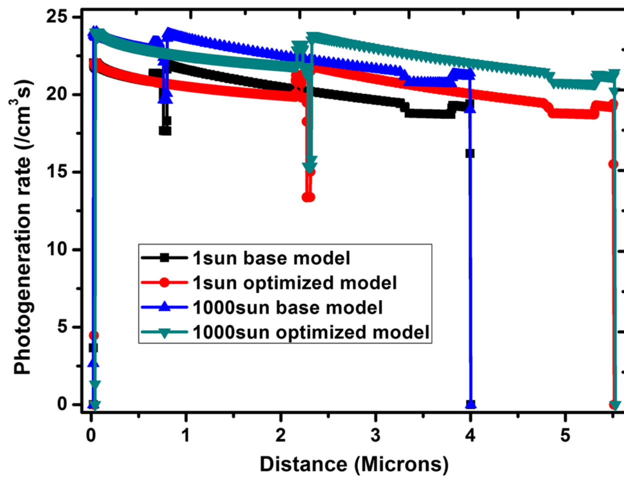

Fig. 14. Cross-sectional view of the photogeneration rate in the proposed model.

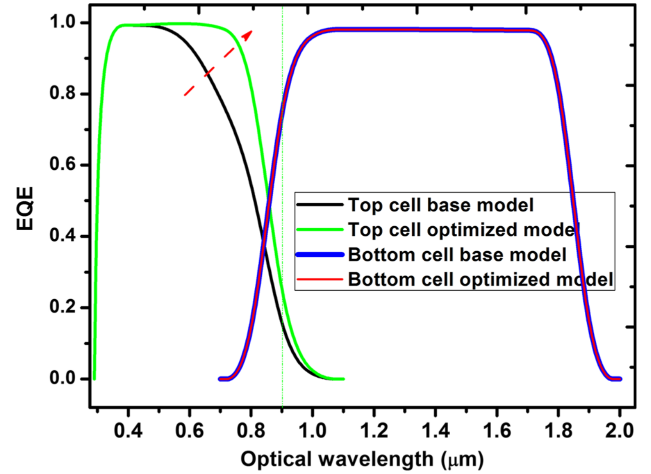

Fig. 15. EQE of the proposed model.

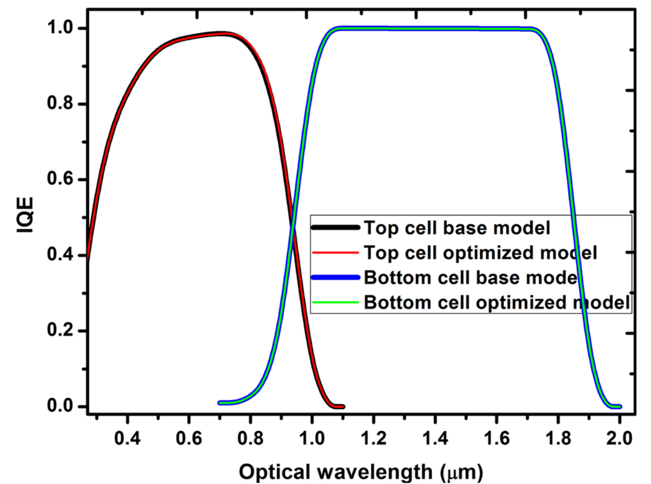

Fig. 16. IQE of the proposed model.

$$EQE(\lambda) = \frac{J_{sc}(\lambda)}{q\phi(\lambda)}, \tag{8}$$

where $J_{sc}(\lambda)$ is the current density, $\phi(\lambda)$ is the photon flux of the light source, and q is the charge on an electron.

According to Fig. 15, the top cell results in a significant improvement in the EQE, due to the higher availability of the photocurrent in the top cell (Fig. 10). Meanwhile, the bottom cell results in a noteworthy expansion in the response (900 nm to 1800 nm) compared with previously reported literature,[19,20,34] where the response of the bottom cell ends at only 900 nm. This change in the EQE is due to the use of GaSb as the active layer in the bottom cell, with a cutoff frequency of 1800 nm. Also from Fig. 14, it can be concluded that the higher photogeneration rate in the bottom cell helps the tandem cell attain an improved EQE compared with other reports in literature.

The IQE can be evaluated mathematically by using the EQE as follows:[19]

$$\text{IQE} = \frac{\text{EQE}}{1 - R(\lambda) - T(\lambda)} = \frac{\Delta J_{sc}}{q\Delta\phi(\lambda)\{1 - R(\lambda) - T(\lambda)\}}, \tag{9}$$

where ΔJ_{sc} is the small improvement in the short-circuit current density for a radiated photon flux of $\Delta\phi(\lambda)$, while $R(\lambda)$ and $T(\lambda)$ are the reflectance and transmittance of the cell, respectively.

The top cell does not show any improvement in the IQE, because the cathode current also improves at the same rate as that of the available photocurrent, leaving the IQE at a constant level (Fig. 10). However, as one moves towards the bottom cell, an IQE of 100% is found up to 1750 nm. The bottom cell made of low-bandgap GaSb consumes the maximum number of photons and generates a large number of electrons and holes, which are transformed into a

cathode current with minimum loss (Fig. 10). This helps the cell to reach higher IQE values.

Reflection and transmission play important roles in the calculation of the IQE and the internal spectral response of the cell. The extracted absorption and transmission for the top and bottom cell with respect to wavelength are shown in Figs. 17 and 18. It can be concluded from Fig. 17 that the top cell absorbs light only up to 900 nm and transmits all other wavelengths, which agrees with the spectral response as well as the EQE and IQE of the top cell. Figure 18 shows that the bottom cell has very low transmittance, whereas it absorbs maximum solar radiation up to 1800 nm and then starts to transmit. This is in full agreement with the spectral response for the bottom cell plotted in Fig. 11.

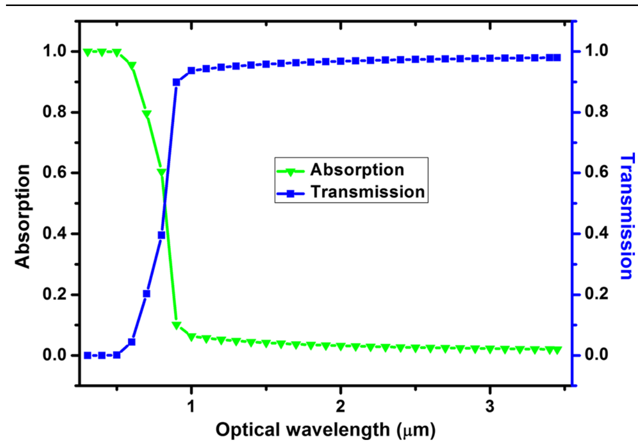

Fig. 17. Absorption and transmission in the top cell.

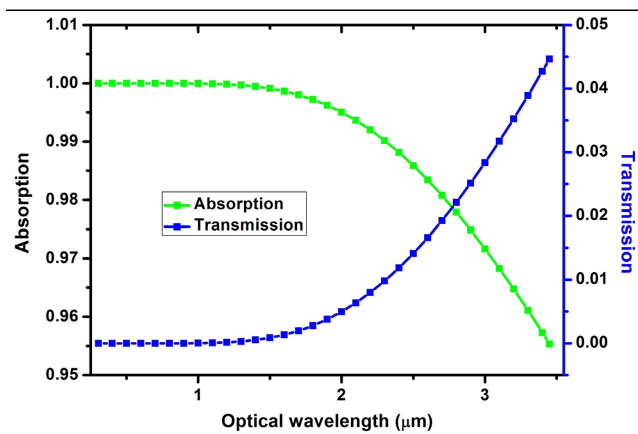

Fig. 18. Absorption and transmission in the bottom cell.

The proposed model was validated by comparing the obtained results with previously reported experimental[18,68] and simulated[34,35,45] results (Table III). For calibration, the I–V curve obtained using the proposed model was compared with that in existing literature for 1 sun[69] and 1000 suns[45] (Fig. 19). The model provides high efficiency due to the high short-circuit current density and higher fill factor, but lower open-circuit voltage due to the use of low-bandgap GaAs in the top cell.

CONCLUSIONS

A highly efficient ARC-less dual-junction solar cell based on low-bandgap materials (GaAs and GaSb) was extensively studied using Silvaco ATLAS TCAD software. The double BSF layer of the top cell, wide-bandgap tunnel interconnect (compared with the bottom cell) with high peak tunneling current, and the wider wavelength response of GaSb make this design much more robust for achieving higher efficiency (> 50%). Parameters such as the efficiency, fill factor, short-circuit current density, and open-circuit voltage of the cell were compared with many previous reports from literature. Other important parameters such as the photogeneration rate, spectral response, EQE, and IQE were discussed to validate the results of the numerical simulations. It was found that, as the bandgap decreases, the photogenerated current increases and the spectral response of the cell increases, resulting in higher efficiency, although the open-circuit voltage of the cell is also affected.

Table III. Comparison table for model validation

Solar cell model	Spectrum	Suns	V_{oc} (V)	J_{sc} (mA/cm^2)	FF (%)	Conv. Eff. (%)
Frass et al.[18]	AM1.5D	100				37.0
Frass et al.[18]	AM0					32.5
Bett et al.[70]	AM1.5D	1	8.73	1155	79.9	23.0
	AM1.5D	100				31.1
Nayak et al.[34]	AM1.5G	1000	2.66	1733	88.67	39.15
Dutta et al.[35]	AM1.5G	1000	2.668	1823	88.29	40.87
Sahoo et al.[45]	AM1.5G	1000	2.66	1898.77	91.17	44.05
This model	AM1.5G	1000	2.25	3182.66	79.058	54.14

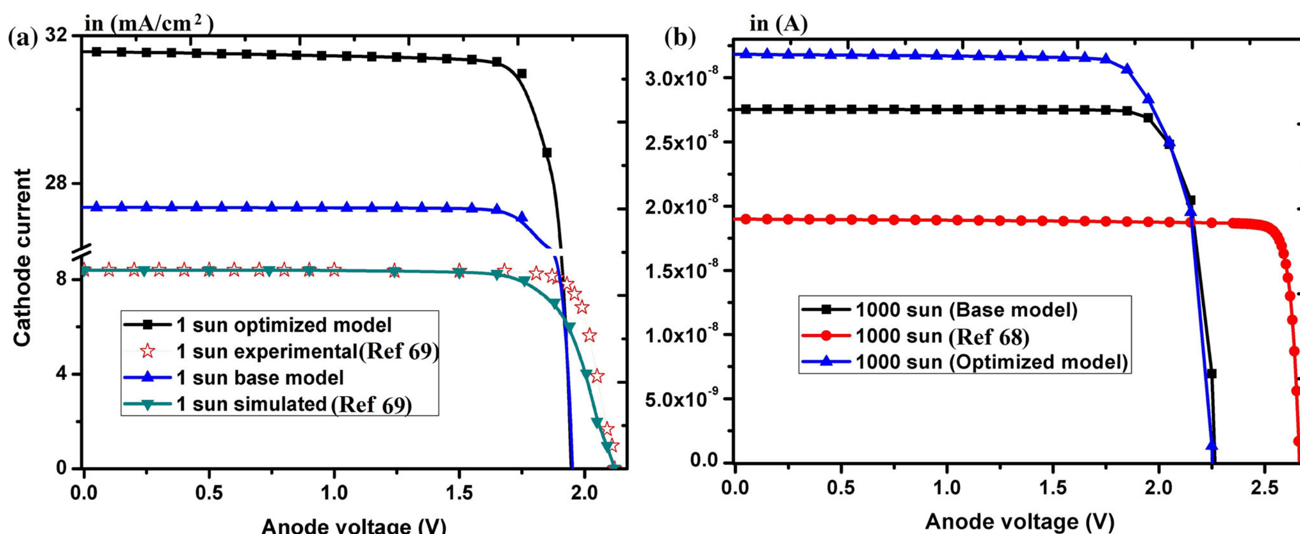

Fig. 19. Comparison of *I–V* curve of the proposed model with literature results for an (a) InGaP/GaAs dual-junction solar cell[69] and (b) InGaP/GaSb dual-junction solar cell.[45]

REFERENCES

1. K. Tanabe, *Energies* 2, 504 (2009).
2. A. Luque and S. Hegedus, *Handbook of Photovoltaic Science and Engineering* (Wiley: Southern Gate, 2003).
3. S.J. Fonash, *Solar Cell Device Physics*, 2nd ed. (Burlington: Academic, 2010).
4. J. M. Roman, in *Advanced Photovoltaic Cell Design*, EN548 (2004), pp. 1–8.
5. W. Shockley and H.J. Queisser, *J. Appl. Phys.* 32, 510 (1961).
6. R. Szweda, *I.I.I.-V. Rev.* 14, 50 (2001).
7. J.M. Olson, D.J. Friedman, and S. Kurtz, High-Efficiency III–V Multijunction Solar Cells, in *Handbook of Photovoltaic Science and Engineering*, 1st ed., A. Luque, S. Hegedus, Eds.; Wiley: New York, NY, USA, (2003) Chapter 9, pp. 359–411.
8. M. McGehee, *Emerging High-Efficiency Low-Cost Solar Cell Technologies.* (Online document).
9. R. Szweda, *Adv. Semicond. Mag.* 16, 53 (2003).
10. M. Yamaguchi, *Energy Procedia* 15, 265 (2012).
11. M. Yamaguchi, *Phys. Status Solidi C* 12, 489 (2015).
12. A.D. Vos, *J. Phys. D Appl. Phys.* 13, 839 (1980).
13. M. Yamaguchi, *Renew. Energy* 8, 354 (1996).
14. M. Yamaguchi, T. Takamoto, K. Araki, and N. Ekins-Daukes, *Sol. Energy* 79, 78 (2005).
15. M.A. Green, K. Emery, Y. Hishikawa, and W. Warta, *Prog. Photovolt. Res. Appl.* 17, 85 (2009).
16. T. Takamoto, E. Ikeda, H. Kurita, and M. Ohmori, *Appl. Phys. Lett.* 70, 381 (1997).
17. I. Garcia, I. Rey-Stolle, B. Galiana, and C. Algora, *Appl. Phys. Lett.* 94, 053509-1 (2009).
18. L.M. Fraas, J.E. Avery, V.S. Sundaram, V.T. Kinh, T.M. Davenport, J.W. Yerkes, J.M. Gee, and K.A. Emery, in *Proceedings of the 21st IEEE Photovoltaic Specialists Conference*, Kissimimee, FL, USA (1990), 190–195.
19. G.S. Sahoo and G.P. Mishra, *Opt. Quant. Electron.* 48, 420 (2016).
20. G.S. Sahoo, P.P. Nayak, and G.P. Mishra, *Superlattices Microstruct.* 95, 115 (2016).
21. G.S. Sahoo and G.P. Mishra, *Procedia Technol.* 25, 684 (2016).
22. K.W.A. Chee and Y. Hu, *Superlattices Microstruct.* 119, 25 (2018).
23. G.S. Sahoo and G.P. Mishra, *Mater. Lett.* 218, 139 (2018).
24. K.W.A. Chee, Z. Tang, H. Lu, and F. Huang, *Energy Rep.* 4, 266 (2018).
25. T. Takamoto, H. Washio, and H. Juso, in *Proceedings of 40th IEEE Photovoltaic Specialists Conference*. New York (2014), pp. 1–5.
26. M. Steiner, G. Siefer, T. Schmidt, M. Wiesenfarth, F. Dimroth, and A.W. Bett, *IEEE J. Photovolt.* 6, 1020 (2016).
27. T.K.P. Luong, V.L. Thanh, A. Ghrib, M.E. Kurdi, and P. Boucaud, *Adv. Nat. Sci.: Nanosci. Nanotechnol.* 6, 015013-1 (2015).
28. L. Fraas, J. Avery, R. Ballantyne, and W. Daniels, *III-Vs Rev.* 12, 22 (1999).
29. I. Bhattacharya, and S.Y. Foo, in *Proceedings of IEEE Southeast Conference, Hyatt Regency Jacksonville,* FL, USA (2013), pp. 1–6.
30. F.H. Alharbi and S. Kais, *Renew. Sustain. Energy Rev.* 43, 1073 (2015).
31. E.B. Elkenany, *Spectrochim. Acta Part A Mol. Biomol. Spectrosc.* 150, 15 (2015).
32. A. Joullie, F.D. Anda, P. Salsac, and M. Mebarki, *Rev. Phys. Appl.* 19, 223 (1984).
33. X. Xianbi, D. Wenhui, C. Xiulan, and L. Xianbo, *Solar Energy Mater. Solar Cells* 55, 313 (1998).
34. P.P. Nayak, J.P. Dutta, and G.P. Mishra, *Eng. Sci. Technol. Int. J.* 18, 325 (2015).
35. J.P. Dutta, P.P. Nayak, and G.P. Mishra, *Optik* 127, 4156 (2016).
36. B.C. Juang, R.B. Laghumavarapu, B.J. Foggo, P.J. Simmonds, A. Lin, B. Liang, and D.L. Huffaker, *Appl. Phys. Lett.* 106, 111101-1 (2015).
37. J.W. Leem, Y.T. Lee, and J.S. Yu, *Opt. Quantum Electron.* 41, 605 (2009).
38. I. Vurgaftman, J.R. Meyer, and L.R. Ram-Mohan, *J. Appl. Phys.* 89, 5815 (2001).
39. SILVACO Data Systems Inc., *Silvaco ATLAS User's Manual* (2010).
40. R.E. Morrison, *Phys. Rev.* 124, 1314 (1961).
41. D.E. Aspnes, S.M. Kelso, R.A. Logan, and R. Bhat, *J. Appl. Phys.* 60, 754 (1986).
42. S. Adachi, H. Kato, A. Moki, and K. Ohtsuka, *J. Appl. Phys.* 75, 478 (1994).
43. H. Kato, S. Adachi, H. Nakanish, and K. Ohtsuka, *Jpn. J. Appl. Phys.* 33, 186 (1994).
44. D.E. Aspnes and A.A. Studna, *Phys. Rev. B*. 27, 985 (1983).
45. G.S. Sahoo and G.P. Mishra, *Superlattices Microstruct.* 109, 794 (2017).
46. K.N. Yaung, M. Vaisman, J. Lang, and M.L. Lee, *Appl. Phys. Lett.* 109, 032107 (2016).

47. M. Vaisman, N. Jain, Q. Li, K.M. Lau, A.C. Tamboli, and E.L. Warren, in *IEEE 44th Photovoltaic Specialists Conference (PVSC)*, Washington, DC (2017), pp. 1–4.
48. N. Jain and M.K. Hudait, *IEEE J. Photovolt.* 3, 528 (2013).
49. I. Garcia, R.M. France, J.F. Geisz, W.E. McMahon, M.A. Steiner, and D.J. Friedman, in *IEEE 42nd Photovoltaic Specialist Conference* (*PVSC*), New Orleans, LA, USA (2015), pp. 1–3.
50. S.A. Ringel, J.A. Carlin, C.L. Andre, M.K. Hudait, M. Gonzalez, D.M. Wilt, E.B. Clark, P. Jenkins, D. Scheiman, A. Allerman, E.A. Fitzgerald, and C.W. Leitz, *Prog. Photovolt: Res. Appl.* 10, 417 (2002).
51. M. Yamaguchi, A. Yamamoto, and Y. Itoh, *J. Appl. Phys.* 59, 1751 (1986).
52. Z. Han, C. NuoFu, W. Yu, Z.X. Wang, Y. Zhi Gang, S. Hui Wei, W.YanSuo, H. Tian Mao, B. Yi Ming, and F. Zhen, *Sci. China Tech. Sci.* 53, 2569 (2010).
53. E.A. Fitzgerald, *Mater. Sci. Rep.* 7, 87 (1991).
54. J.A. Carlin, S.A. Ringel, A. Fitzgerald, and M. Bulsara, *Sol. Energy Mater. Sol. Cells* 66, 621 (2001).
55. S.M. Vernon, S.P. Tobin, M.M. Al-Jassim, R.K. Ahrenkiel, K.M. Jones, and B.M. Keyes, in *Proceedings of 21st IEEE Photovoltaic Specialists Conference, Kissimmee*, FL, USA (1990), pp. 211–216.
56. M. Yamaguchi, A. Yamamoto, and Y. Itoh, *J. Appl. Phys.* 59, 1751 (1986).
57. M. Yamaguchi, C. Amano, and Y. Itoh, *J. Appl. Phys.* 66, 915 (1989).
58. C.L. Andre, D.M. Wilt, A.J. Pitera, M.L. Lee, E.A. Fitzgerald, and S.A. Ringel, *J. Appl. Phys.* 98, 014502 (2005).
59. J.C. Zolper and A.M. Barnett, *IEEE Trans. Electron Devices* 37, 478 (1990).
60. Online document, Available: http://energyprofessionalsymposium.com/?p=6031. Accessed 11 Jan 2018.
61. S.H. Huynh, M.T.H. Ha, H.B. Do, Q.H. Luc, H.W. Yu, and E.Y. Chang, *Appl. Phys. Lett.* 109, 102107 (2016).
62. A. Jallipalli, G. Balakrishnan, S.H. Huang, T.J. Rotter, K. Nunna, B.L. Liang, L.R. Dawson, and D.L. Huffaker, *Nanoscale Res. Lett.* 4, 1458 (2009).
63. G.T. Nelson, B.C. Juang, M.A. Slocum, Z.S. Bittner, R.B. Laghumavarapu, D.L. Huffaker, and S.M. Hubbard, *Appl. Phys. Lett.* 111, 231104 (2017).
64. A. Mansoori, S.J. Addamane, E.J. Renteria, D.M. Shima, M. Behzadirad, E. Vadiee, C. Honsberg, and G. Balakrishnan, *Solar Energy Mater. Solar Cells* 185, 21 (2018).
65. D. Benyahia, L. Kubiszyn, K. Michalczewski, A. Keblowski, P. Martyniuk, J. Piotrowski, and A. Rogalski, *Opto-Electron. Rev.* 24, 40 (2016).
66. S.H. Huang, G. Balakrishnan, A. Khoshakhlagh, A. Jallipalli, L.R. Dawson, and D.L. Huffaker, *Appl. Phys. Lett.* 88, 131911 (2006).
67. A. P. Kirk, *Solar Photovoltaic Cells Photons to Electricity* (Academic, Elsevier Inc. 2015).
68. L.M. Fraas, J.E. Avery, J. Martin, V.S. Sundaram, G. Girard, V.T. Dinh, T.M. Davenport, J.W. Yerkes, and M.J. O'Neill, *IEEE Trans. Electron Devices* 37, 443 (1990).
69. M. Baudrit and C. Algora, in *33rd IEEE PVSC*, San Diego, CA (2008), pp. 1–5.
70. A.W. Bett, S. Keser, G. Stollwerck, O.V. Sulima, and W. Wettling, in *26th PVSC*, Anaheim, CA (1997), pp. 931–934.